IEEE Access
Multidisciplinary | Rapid Review | Open Access Journal

Received 27 December 2024, accepted 24 January 2025, date of publication 7 February 2025, date of current version 14 February 2025.

Digital Object Identifier 10.1109/ACCESS.2025.3539925

RESEARCH ARTICLE

A Detailed Analytical Modeling of Eddy Current Losses in an Underwater Medium for Wireless Power Transfer

SADJAD SHAFIEI[1], SEYED SAEID HEIDARI YAZDI[1], NURTAS ADAIKHAN[2], AND MEHDI BAGHERI[1], (Senior Member, IEEE)

[1]Department of Electrical and Computer Engineering, School of Engineering and Digital Sciences, Nazarbayev University, Astana 010000, Kazakhstan
[2]Faculty of Mechanics and Mathematics, L. N. Gumilyov Eurasian National University, Astana 010008, Kazakhstan

Corresponding author: Mehdi Bagheri (mehdi.bagheri@nu.edu.kz)

This work was supported in part by the Collaborative Research Project (CRP), Nazarbayev University, under Grant 211123CRP1604; and in part by the Faculty Development Competitive Research Grant (FDCRG), Nazarbayev University, under Grant 201223FD8811.

ABSTRACT Eddy current loss (ECL) in underwater wireless power transfer (UWPT) systems can significantly affect the efficiency of underwater vehicles. This study provides comprehensive modeling of the eddy current effects in circular planar coils. The analytical model has been extended to any number of transmitter and receiver coils' turns exposed to different conductive regions, providing a general formulation applicable to various scenarios. From the circuit perspective, ECLs appear as the additional resistances in both primary and secondary coils, as well as the newly introduced mutual resistance that in turn contributes to power loss. To derive the general formulas for additional resistances, the electric field intensities are calculated by solving the Helmholtz equation within different surrounding environments, considering geometrical parameters such as the number of turns, coil radii, and spacing between turns. Three frequently occurring scenarios in underwater applications are selected to provide a comprehensive understanding of ECLs. The general formulas are solved by properly defining the boundary condition, and then the additional resistances are calculated specifically for each scenario. Finite Element Method (FEM) simulations and measurements are conducted to validate the analytical formulation. The results confirm the high accuracy and reliability of the model. It effectively captures the impact of changes in the geometrical parameters of the coils on additional resistances, well predicts the effect of increasing the input source frequency, and demonstrates how the effects of eddy currents change with the volume of the surrounding conductive medium.

INDEX TERMS Eddy current loss, electric boat, Helmholtz equation, mutual resistances, planar coil, resistance variations, underwater wireless power transfer.

I. INTRODUCTION

For decades, the mysterious habitat of the seabed remained unexplored. Scientists have always been scouring this dismal world. The seafloor is home to a large population of marine life, which is essential for the ecosystem. Moreover, the natural resources are reserved beneath the seafloor accounting for a considerable share of natural resources worldwide. However, to discover and unearth these valuable resources yet ensure the preservation of marine life requires recruiting new emerging technologies.

Regarding underwater technology, submersed devices such as remotely operated vehicles, submerged buoys, etc., are frequently used for this purpose [1], [2], [3]. Compared to traditional battery charging methods, in recent years wirelessly power delivery techniques have gained significant attention for underwater devices due to their enhanced safety and higher reliability. Among the various wireless power transfer (WPT) techniques, two near-field approaches, magnetically-driven and electrically-driven are the most

The associate editor coordinating the review of this manuscript and approving it for publication was Diego Masotti.

common. Inductive wireless power transfer (IWPT) is more prevalent than its traditional competitor. However, since IWPT works with high-frequency alternative magnetic fields, the eddy current loss (ECL) or Foucault currents is initiated within the conductive coupling medium as claimed by Lenz's law.

Researchers have conducted studies that include introducing novel coil configurations [4] and employing current control techniques [5] to mitigate the effects of ECLs. Frequency is a crucial factor in the generating of ECLs, require regulations to achieve better performance [6]. Beyond these efforts, modeling of ECLs by analyzing the electric field intensities within the surrounding conductive medium enhances understanding of ECLs and identifies key influencing factors. ECL modeling depends on the geometry of the coils and the electromagnetic properties of the surrounding conductive environment. For complex structures with non-uniform and heterogeneous environments, directly calculating of ECLs becomes mathematically complicated. In [7], the numerical method has been employed to investigate the effect of the existing non-uniform and heterogeneous conductive medium in the flux path of planar coils with a domino arrangement.

Circular planar coils are commonly used in many WPT systems, with various power ranges. This kind of coil structure has also been utilized in underwater applications. The conductive medium of flux path is always a stumbling block to achieving higher efficiency in the UWPT systems and complicates the design procedure. Water can be considered a uniform and homogeneous medium, allowing for the direct calculation of ECLs using precise mathematical models. Thereby, ECLs are estimated by solving the Helmholtz equation in the cylindrical coordinate system for electric field intensity in a water medium. The electric fields for a pair of current loops are straightforward to calculate [8] and can be extended to any number of loops [9]. ECLs are influenced by the location of the coils, the coupling distance, and the boundary conditions. In a UWPT system with two circular planar coils, the surrounding area is divided into three subregions to compute the electric field intensities. In [10] ECLs are derived for one pair of fully submerged single-turn coils and all three subregions exhibit the same properties. In [11] one region is considered to be air and the other two regions have the same properties and ECLs are derived for one pair of single-turn coils. In [12] the water region is limited between two coils and the other two have identical properties.

Research Gap: Existing literature lacks a comprehensive analysis of the impact of eddy currents on the resistance of planar coils and the influence of geometrical parameters on resistance variations in conductive environments. Based on findings from [10], [11], and [12], it is evident that three boundary conditions commonly occur in UWPT systems. This study provides an in-depth analysis of all three scenarios and generalizes the derived formulas for ECLs, considering any number of transmitter and receiver coil turns in different conductive regions. The generalized equations provide a versatile framework that can be applied to different scenarios, enabling the extraction of specific equations for ECLs corresponding to each of the three boundary conditions discussed in [10], [11], and [12]. This research fills the identified gap in the literature through the following contributions:

First Contribution: A comprehensive model has been developed to calculate the additional resistances arising from the eddy current effects in circular planar coils. The analytical model has been extended to any number of transmitter and receiver coils' turns exposed to three conductive subregions, each with different properties, providing a general formulation applicable to various scenarios.

Second Contribution: The additional resistances are calculated using the general formulas for each specific scenario. The formulas account for the geometrical parameters, the effect of frequency, and the influence of the surrounding conductive medium. A comparison is then conducted to investigate how variations in geometrical parameters–key design factors of a UWPT system–affect the additional resistances at different frequencies.

Third Contribution: In addition to the additional resistances, the electric field distribution within each conductive medium is calculated separately for each scenario. The electric fields from each subregion are then integrated into a single plot to demonstrate that only the circumferential component contributes to the electric field distribution and the associated additional resistances. The plots from the calculations are compared with FEM results for two frequencies: one low and one relatively high, to verify the accuracy of the model.

Regarding the logical flow of this research, Section II provides a general overview of the studied system. The surrounding environment is divided into three conductive subregions, each with distinct characteristics, and these subregions are separated by coils placed at the boundaries. The electric field is calculated in each of these areas, and by calculating the induced voltage in each of the planar coils, general formulas are derived to determine the additional resistances. In Section III, the properties of water are considered as a conductive medium, and the additional resistances for three commonly occurring scenarios in underwater applications are specifically calculated. The accuracy of the model is assessed in the final section by examining the effect of changes in operating frequency and the geometrical parameters of the coils. Moreover, the electric fields obtained in Section II are plotted for two different frequencies to validate the model's accuracy and demonstrate that only the circumferential component of the electric field contributes to the calculations.

II. EDDY CURRENT LOSS MODELING

The electric field intensity in the conductive medium of the coils is required to determine the ECLs. The following assumptions are considered to simplify the analytical computation.

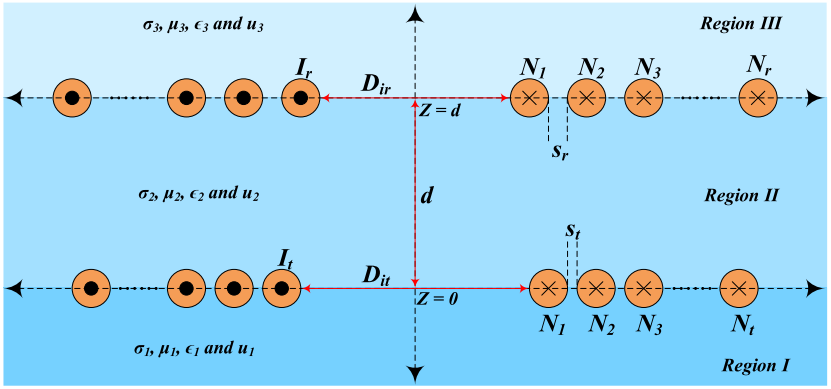

FIGURE 1. Region divisions and the location of coaxial circular planar coils at the boundaries in the cylindrical coordinate system.

1) The properties of seawater are consistent throughout the medium and are presumed to be linear, isotropic, and uniform.
2) The seawater is unbounded in XY-plane.
3) The geometry of coils is circular and planar.
4) The number of strands so that the wire diameter is not included in the modeling.
5) The misalignment is not included in the modeling, and both coils are aligned on Z-axis.
6) A sinusoidal, current source is applied to both coils.

A. ELECTRIC FIELD INTENSITY

The electric field intensity can be obtained using the following Maxwell's equations:

$$\begin{cases} \nabla \times \mathbf{E}_{ij} = -\dfrac{\partial \mathbf{B}_{ij}}{\partial t} \\ \nabla \times \mathbf{H}_{ij} = \mathbf{J}_{ij} + \dfrac{\partial \mathbf{D}_{ij}}{\partial t}, \quad i = t, r \quad j = 1, 2, 3 \\ \mathbf{J}_{ij} = \sigma_j \mathbf{E}_{ij}, \quad \mathbf{D}_{ij} = \epsilon_j \mathbf{E}_{ij}, \quad \mathbf{B}_{ij} = \mu_j \mathbf{H}_{ij} \end{cases} \tag{1}$$

where $i = t, r$ represents the transmitter and receiver, respectively, while j indexes the subregions. The vectors $\mathbf{H}_{ij}$ and $\mathbf{B}_{ij}$ denote the magnetic field intensity and magnetic flux density of the i-th coil in the j-th region in Fig. 1, respectively. Similarly, $\mathbf{E}_{ij}$ and $\mathbf{J}_{ij}$ refer to the electric field intensity and current density of the i-th coil within the j-th region. The electric displacement vector is represented by $\mathbf{D}_{ij}$. The properties of the regions are characterized by σ_j, ϵ_j, and μ_j, which correspond to conductivity, permittivity, and permeability, respectively. By performing the appropriate mathematical operations on (1), the following expression known as Helmholtz equation for the electric field intensity can be expressed as:

$$\nabla^2 \mathbf{E}_{ij} + k_j^2 \mathbf{E}_{ij} = 0 \tag{2}$$

where $k_j^2 = \mu_j \omega(\epsilon_j \omega - j\sigma_j)$ known as the space wave number, and is a function of the surrounding medium and frequency of applied currents. Due to the symmetric geometry of the circular planar coils in the cylindrical coordinate system and the circular current path, the component of $\mathbf{E}_{ij}$ in radius ($E_{ijr}\hat{e}_r$) and axial ($E_{ijz}\hat{e}_z$) directions can be neglected. Therefore (2) in a cylindrical coordinate system can be shown as:

$$\frac{\partial^2 E_{ij\phi}}{\partial z^2} + \frac{\partial^2 E_{ij\phi}}{\partial r^2} + \frac{1}{r}\left(\frac{\partial E_{ij\phi}}{\partial r}\right) + \left(\mu_j \omega(\epsilon_j \omega - j\sigma_j) - \frac{1}{r^2}\right) E_{ij\phi} = 0 \tag{3}$$

As indicated by (3), the electric field intensity varies along the z-axis and the radial direction. Through using the variable separation method $E_{ij\phi}(r, z) = R(r)Z(z)$ and substitute in (2) [12], the general expression for $R(r)$ and $Z(z)$ are obtained by

$$\begin{cases} R(r, \tau) = a_{ij}(\tau) J_1(r\tau) + b_{ij}(\tau) Y_1(r\tau) \\ Z(z, \tau) = c_{ij}(\tau) e^{u_j(z - z_i)} + d_{ij}(\tau) e^{-u_j(z - z_i)} \end{cases} \tag{4}$$

where $J_1(r\tau)$ and $Y_1(r\tau)$ are the first and second kind for the first-order Bessel function, respectively. $u_j = \sqrt{\tau^2 - \mu_j \omega(\epsilon_j \omega - j\sigma_j)}$, and it is a function of the surrounding medium and frequency of applied currents. z_i shows the location of $i - th$ coil in XY-plane. The variable τ serves as the separation constant value and varies for $\tau \geq 0$.

Finally, the general solution to (3) can be obtained by integrating the electric field intensity over the variable τ.

$$E_{ij\phi}(r, z) = \int_0^\infty \left(a_{ij}(\tau) J_1(r\tau) + b_{ij}(\tau) Y_1(r\tau)\right) \times \left(c_{ij}(\tau) e^{u_j(z - z_i)} + d_{ij}(\tau) e^{-u_j(z - z_i)}\right) d\tau \tag{5}$$

This equation illustrates the electric field intensity generated by $i - th$ coil in $j - th$ region. According to the property of Y_1 the value of $\lim_{\tau \to 0} Y_1(r\tau) = -\infty$ is unbounded, whereas the electric field intensity is bounded and nonzero, hence $b_{ij}(\tau) = 0$. Therefore,

$$E_{ij\phi}(r, z) = \int_0^\infty J_1(r\tau)\left(a'_{ij}(\tau) e^{u_j(z - z_i)} + a''_{ij}(\tau) e^{-u_j(z - z_i)}\right) d\tau \tag{6}$$

where $a'_{ij}(\tau) = a_{ij}(\tau)c_{ij}(\tau)$ and $a''_{ij}(\tau) = a_{ij}(\tau)d_{ij}(\tau)$. The goal is to solve (6) for three different case studies defined in Fig. 2. The boundary conditions are required in each case to determine the coefficients. To solve (6), the superposition theorem is applied to each coil independently. The electric field intensity is calculated in three subregions for each coil.

I) In the area beneath the transmitter coil ($j = 1$), since $\lim_{(z-z_i)\to-\infty} E_{ij\phi} = 0$, therefore the parameters $a''_{t1}(\tau)$ and $a''_{r1}(\tau) = 0$. The electric field intensity by the transmitter ($z_i = 0, z \to -\infty$) and by the receiver ($z_i = d$, $(z-d) \to -\infty$) is:

$$\begin{cases} E_{t1\phi}(r,z) = \displaystyle\int_0^\infty a'_{t1}(\tau)J_1(r\tau)e^{u_1 z}d\tau \\ E_{r1\phi}(r,z) = \displaystyle\int_0^\infty a'_{r1}(\tau)J_1(r\tau)e^{u_1(z-d)}d\tau \end{cases} \tag{7}$$

II) In the region between the two coils ($j = 2$), z is limited ($0 \le z \le d$), both decreasing and increasing exponential components appear in the electric field intensity equation:

$$\begin{cases} E_{t2\phi}(r,z) = \displaystyle\int_0^\infty J_1(r\tau)\Big(a'_{t2}(\tau)e^{u_2 z} + a''_{t2}(\tau)e^{-u_2 z}\Big)d\tau \\ E_{r2\phi}(r,z) = \displaystyle\int_0^\infty J_1(r\tau) \times \Big(\\ \qquad a'_{r2}(\tau)e^{u_2(z-d)} + a''_{r2}(\tau)e^{-u_2(z-d)}\Big)d\tau \end{cases} \tag{8}$$

III) In the region above the receiver coil ($j = 3$), since $\lim_{(z-z_i)\to+\infty} E_{ij\phi} = 0$, therefore the parameters $a'_{t3}(\tau)$ and $a'_{r3}(\tau) = 0$. The electric field intensity for the transmitter ($z_i = 0, z \to +\infty$) and for the receiver ($z_i = d$, $(z-d) \to +\infty$) is:

$$\begin{cases} E_{t3\phi}(r,z) = \displaystyle\int_0^\infty a''_{t3}(\tau)J_1(r\tau)e^{-u_3 z}d\tau \\ E_{r3\phi}(r,z) = \displaystyle\int_0^\infty a''_{r3}(\tau)J_1(r\tau)e^{-u_3(z-d)}d\tau \end{cases} \tag{9}$$

The boundary conditions are required to determine the remaining coefficients in (7)-(9). The following relations describe the behavior of the electric field intensity at the boundary of adjacent regions

$$\begin{cases} E_{i1\phi}(r,z) = E_{i2\phi}(r,z), \quad z = 0 \\ E_{i2\phi}(r,z) = E_{i3\phi}(r,z), \quad z = d \\ \dfrac{\partial}{\partial z}(E_{i2\phi} - E_{i1\phi}) = j\omega\mu_0 I_{im}\delta(r - a_{im}), \quad z = 0 \\ \dfrac{\partial}{\partial z}(E_{i3\phi} - E_{i2\phi}) = j\omega\mu_0 I_{in}\delta(r - a_{in}), \quad z = d \end{cases} \tag{10}$$

Here, I_{im} and I_{in} denote the currents flowing through the m-th and n-th current loops with radii of a_{im} and a_{in} for the coils located at the boundaries $z = 0$ and $z = d$, respectively. It is evident that, for the transmitter and receiver coils at the boundaries of $z = d$ and $z = 0$, the values of currents $I_{in} = 0$ and $I_{im} = 0$, respectively. The electric field intensity is a function of Bessel functions, to equalize the derivatives of the electric field intensities in (10) with a $\delta-$function it is required to represent $\delta-$function in terms of Bessel functions as below [13]:

$$\int_0^\infty \tau J_i(r\tau)J_i(a\tau)d\tau = \frac{1}{r}\delta(r-a) \tag{11}$$

Therefore, all coefficients can be determined utilizing (7)-(10).

$$\begin{cases} a'_{t1}(\tau) = p(\tau)\Big((u_2+u_3)e^{u_2 d} + (u_2-u_3)e^{-u_2 d}\Big) \\ a'_{t2}(\tau) = p(\tau)(u_2-u_3)e^{-u_2 d} \\ a''_{t2}(\tau) = p(\tau)(u_2+u_3)e^{u_2 d} \\ a''_{t3}(\tau) = 2p(\tau)u_2 e^{u_3 d} \end{cases} \tag{12}$$

and

$$\begin{cases} a'_{r1}(\tau) = 2q(\tau)u_2 e^{u_1 d} \\ a'_{r2}(\tau) = q(\tau)(u_2+u_1)e^{u_2 d} \\ a''_{r2}(\tau) = q(\tau)(u_2-u_1)e^{-u_2 d} \\ a''_{r3}(\tau) = q(\tau)\Big((u_2+u_1)e^{u_2 d} + (u_2-u_1)e^{-u_2 d}\Big) \end{cases} \tag{13}$$

where $p(\tau)$ and $q(\tau)$ are as follows

$$\begin{cases} p = \dfrac{j\omega\mu_0 I_{tm}a_{tm}\tau J_1(a_{tm}\tau)}{(u_2-u_3)(u_2-u_1)e^{-u_2 d} - (u_2+u_1)(u_2+u_3)e^{u_2 d}} \\ q = \dfrac{j\omega\mu_0 I_{rn}a_{rn}\tau J_1(a_{rn}\tau)}{(u_2-u_3)(u_2-u_1)e^{-u_2 d} - (u_2+u_1)(u_2+u_3)e^{u_2 d}} \end{cases} \tag{14}$$

B. OPEN CIRCUIT VOLTAGE

The electric field intensity varies with the current flowing through the coils. By employing (15), the link between induced voltage and coils' current is established, enabling the calculation of additional resistances caused by eddy current losses. The induced open circuit voltages in $m-th$ and $n-th$ single turn with the lengths of l_m and l_n for transmitter and receiver, respectively are:

$$\begin{cases} U_{tm} = -\displaystyle\int_{l_m} \mathbf{E}_{2\phi}(r,z)\Big|_{z=0, r=a_{tm}} dl \\ U_{rn} = -\displaystyle\int_{l_n} \mathbf{E}_{2\phi}(r,z)\Big|_{z=d, r=a_{rn}} dl \end{cases} \tag{15}$$

where $\mathbf{E}_{2\phi}$ is the equivalent electric field intensity in the region between coils and is obtained by

$$\mathbf{E}_{2\phi}(r,z) = \sum_{m=1}^{N_t} \mathbf{E}_{t2\phi m}(r,z) + \sum_{n=1}^{N_r} \mathbf{E}_{r2\phi n}(r,z) \tag{16}$$

where $\mathbf{E}_{t2\phi m}$ and $\mathbf{E}_{r2\phi n}$ are the circumferential components of the electric field intensity for the $m-th$ and $n-th$ turns of the transmitter and receiver coils, respectively, in the second region. The sum of the induced voltages in all adjacent turns of each coil represents the total value of induced voltage. Substituting (16) in (15), the total induced open circuit

voltage for each coil will be

$$\begin{cases} U_t = -2\pi \sum_{m=1}^{N_t} a_{tm} E_{2\phi}(a_{tm}, 0) \\ U_r = -2\pi \sum_{n=1}^{N_r} a_{rn} E_{2\phi}(a_{rn}, d) \end{cases} \tag{17}$$

Since in the water region, the conductivity is $\sigma_j \neq 0$, therefore, k_j^2 has both real and imaginary parts, thereby, the induced voltage can be written in the following form:

$$\begin{cases} U_t = (R_{et} + j\omega L_t)\, I_t + (R_{etr} + j\omega M)\, I_r \\ U_r = (R_{etr} + j\omega M)\, I_t + (R_{er} + j\omega L_r)\, I_r \end{cases} \tag{18}$$

where R_{et}, R_{er} and R_{etr} are the additional resistances reflecting the eddy currents. Moreover, $I_{t1} = I_{t2} = \ldots = I_{tm} = I_t$ and $I_{r1} = I_{r2} = \ldots = I_{rn} = I_r$.

C. ADDITIONAL RESISTANCES

As seen in (18), the eddy currents contribute the additional terms to the real part of the impedances, these additional terms are calculated independently as follows:

$$\begin{cases} R_{et} = Real\left\{\dfrac{U_t}{I_t}\right\}_{I_r=0} \\ R_{er} = Real\left\{\dfrac{U_r}{I_r}\right\}_{I_t=0} \\ R_{etr} = Real\left\{\dfrac{U_t}{I_r}\right\}_{I_t=0} = Real\left\{\dfrac{U_r}{I_t}\right\}_{I_r=0} \end{cases} \tag{19}$$

Using (8), and (12)-(19) the additional parts can be derived (see (20)-(22)), as shown at the bottom of the next page. As can be seen, the additional resistances in each coil are influenced by the environmental characteristics of all three regions (u_1, u_2 and u_3). Moreover, according to (22), the mutual resistance decreases with increasing distance d, and eventually drops to zero. Additionally, the presence of the parameter d in self-resistances can be explained by the extent to which the second region, characterized by u_2, influences self-resistances. Therefore, logically, the effect of the parameter d appears in the self-resistance equations.

III. COMPARISON OF DIFFERENT CONDITIONS

Here three different case studies are analyzed, and the additional resistances are derived for each of them.

A. INFINITE MEDIUM

For the first case study in Fig. 2(a), the water region infinitely expands in all directions, hence we can assume that $u_1 = u_2 = u_3 = u_w$, $I_{tm} = I_t$, $I_{rn} = I_r$. Using (20)-(22) the additional resistances in the real part of impedances for fully-submerged coils are:

$$R_{et} = Real\left\{ j\omega\mu_0\pi \times \sum_{m=1}^{N_t}\sum_{k=1}^{N_t} a_{tm}a_{tk} \int_0^\infty \frac{\tau J_1(a_{tm}\tau)J_1(a_{tk}\tau)}{u_w} d\tau \right\} \tag{23}$$

$$R_{er} = Real\left\{ j\omega\mu_0\pi \times \sum_{n=1}^{N_r}\sum_{k=1}^{N_r} a_{rn}a_{rk} \int_0^\infty \frac{\tau J_1(a_{rn}\tau)J_1(a_{rk}\tau)}{u_w} d\tau \right\} \tag{24}$$

and for the mutual additional resistance

$$R_{etr} = Real\left\{ j\omega\mu_0\pi \times \sum_{m=1}^{N_t}\sum_{n=1}^{N_r} a_{tm}a_{rn} \int_0^\infty \frac{\tau J_1(a_{tm}\tau)J_1(a_{rn}\tau)}{u_w e^{u_w d}} d\tau \right\} \tag{25}$$

Since the characteristics of all three regions are the same as each other, there is no effect of d on additional self-resistances. Additionally, (25) demonstrates that mutual resistances decrease as the distance between the two coils increases.

B. SEMI-FINITE MEDIUM

The semi-finite medium in this study refers to a region where the water infinitely expands in the XY-plane and is limited for $z \leq 0$ (see Fig. 2(b)). Hence, $u_1 = u_a$, $u_2 = u_3 = u_w$, $I_{tm} = I_t$, $I_{rn} = I_r$. Using (20)-(22), the additional resistances appearing in the real part of the impedances are:

$$R_{et} = Real\left\{ 2j\omega\mu_0\pi \times \sum_{m=1}^{N_t}\sum_{k=1}^{N_t} a_{tm}a_{tk} \int_0^\infty \frac{\tau J_1(a_{tm}\tau)J_1(a_{tk}\tau)}{u_w + u_a} d\tau \right\} \tag{26}$$

$$R_{er} = Real\left\{ j\omega\mu_0\pi \sum_{n=1}^{N_r}\sum_{k=1}^{N_r} a_{rn}a_{rk} \int_0^\infty \tau J_1(a_{rn}\tau) \times J_1(a_{rk}\tau) \frac{u_w + u_a + (u_w - u_a)e^{-2u_w d}}{u_w(u_w + u_a)} d\tau \right\} \tag{27}$$

and for the mutual additional resistance

$$R_{etr} = Real\left\{ 2j\omega\mu_0\pi \times \sum_{m=1}^{N_t}\sum_{n=1}^{N_r} a_{tm}a_{rn} \int_0^\infty \frac{\tau J_1(a_{tm}\tau)J_1(a_{rn}\tau)}{(u_w + u_a)e^{u_w d}} d\tau \right\} \tag{28}$$

Here, because the characteristics of the second and third environments are the same, changes in distance will not affect the additional resistance of the transmitter coil, and according to (26), no effect of the parameter d is seen. On the other hand, parameter d appears in the expression related to the additional self-resistance of the receiver coil. This indicates how close the second coil is to the first region. Therefore, the smaller d is, the closer the coil is to the boundary of the first region, resulting in less effect of the eddy currents and a more prominent impact of the first region's characteristics.

C. FINITE MEDIUM

In this case, the water region infinitely expands in the XY-plane and is limited in $0 \leq z \leq d$ (see Fig. 2(c)). Here

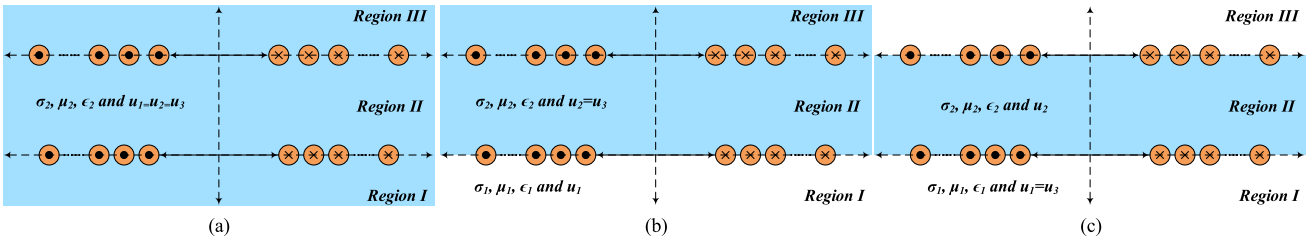

FIGURE 2. Region divisions for three different boundary conditions at the z-axis. (a) Infinite medium (b) Semi-finite medium (c) Finite medium.

regions 1 and 3 are assumed to be as air, $u_1 = u_3 = u_a$, and region 2 is water $u_2 = u_w$, $I_{tm} = I_t$, and $I_{rn} = I_r$. Using (20)-(22), the additional resistances appearing in the real part of the impedances are:

$$R_{et} = Real\left\{-2j\omega\mu_0\pi \sum_{m=1}^{N_t}\sum_{k=1}^{N_t} a_{tm}a_{tk}\int_0^\infty \tau J_1(a_{tm}\tau) \times J_1(a_{tk}\tau)\frac{(u_w+u_a)e^{u_w d}+(u_w-u_a)e^{-u_w d}}{(u_w-u_a)^2e^{-u_w d}-(u_w+u_a)^2e^{u_w d}}d\tau\right\} \tag{29}$$

and for the receiver coil

$$R_{er} = Real\left\{-2j\omega\mu_0\pi \sum_{n=1}^{N_r}\sum_{k=1}^{N_r} a_{rn}a_{rk}\int_0^\infty \tau J_1(a_{rn}\tau) \times J_1(a_{rk}\tau)\frac{(u_w+u_a)e^{u_w d}+(u_w-u_a)e^{-u_w d}}{(u_w-u_a)^2e^{-u_w d}-(u_w+u_a)^2e^{u_w d}}d\tau\right\} \tag{30}$$

the additional mutual resistance is

$$R_{etr} = Real\left\{-4j\omega\mu_0\pi \sum_{m=1}^{N_t}\sum_{n=1}^{N_r} a_{tm}a_{rn}\int_0^\infty \tau J_1(a_{tm}\tau) \times J_1(a_{rn}\tau)\frac{u_w}{(u_w-u_a)^2e^{-u_w d}-(u_w+u_a)^2e^{u_w d}}d\tau\right\} \tag{31}$$

The presence of the parameter d in the self-resistances can be justified by considering that the degree of influence of the second region, characterized by u_2, and depends on its height. Therefore, logically, its effect appears in the relationships. Moreover, as illustrated in (31), the mutual resistance decreases with increasing distance d, and eventually drops to zero.

TABLE 1. Main parameters of the circular planar coils along with the electric and magnetic properties of water region.

Items	Symbol	Value
Main parameters of coils		
Number of turns	N_t/N_r	15/17
Inner diameter (mm)	D_{it}/D_{ir}	170/165
Space turn (mm)	s_t/s_r	1/1
Number of strands	n_{str}	160
Wire diameter (mm)	d_w	1.5
Properties of coupling medium		
Conductivity (S/m)	σ	4
Permittivity	ϵ_r	81
Permeability	μ_r	≈ 1

IV. RESULTS AND FINDINGS

The additional resistances and subsequently the additional losses depend on the geometric characteristics of the coils, including the radius (r) and the number of turns (N). The radius itself depends on the distance (s) between adjacent turns (see Fig. 1). These parameters can be considered independent variables. Hence, a comparison is conducted to examine the impact of variations in each of the independent variables of the coils' geometry and the applied frequency on the ECLs.

A. FREQUENCY IMPACT

The impact of varying the applied current's frequency on the additional resistances is illustrated in Figs. 3-5, where the analytical modeling is compared with FEM simulations and laboratory measurements. To verify the accuracy of

$$R_{et} = Real\left\{-2j\omega\mu_0\pi \sum_{m=1}^{N_t}\sum_{k=1}^{N_t} a_{tm}a_{tk}\int_0^\infty \frac{\left((u_2+u_3)e^{u_2 d}+(u_2-u_3)e^{-u_2 d}\right)\tau J_1(a_{tm}\tau)J_1(a_{tk}\tau)}{(u_2-u_3)(u_2-u_1)e^{-u_2 d}-(u_2+u_1)(u_2+u_3)e^{u_2 d}}d\tau\right\} \tag{20}$$

$$R_{er} = Real\left\{-2j\omega\mu_0\pi \sum_{n=1}^{N_r}\sum_{k=1}^{N_r} a_{rn}a_{rk}\int_0^\infty \frac{\left((u_2+u_1)e^{u_2 d}+(u_2-u_1)e^{-u_2 d}\right)\tau J_1(a_{rn}\tau)J_1(a_{rk}\tau)}{(u_2-u_3)(u_2-u_1)e^{-u_2 d}-(u_2+u_1)(u_2+u_3)e^{u_2 d}}d\tau\right\} \tag{21}$$

$$R_{etr} = Real\left\{-4j\omega\mu_0\pi \sum_{m=1}^{N_t}\sum_{n=1}^{N_r} a_{tm}a_{rn}\int_0^\infty \frac{u_2\tau J_1(a_{tm}\tau)J_1(a_{rn}\tau)}{(u_2-u_3)(u_2-u_1)e^{-u_2 d}-(u_2+u_1)(u_2+u_3)e^{u_2 d}}d\tau\right\} \tag{22}$$

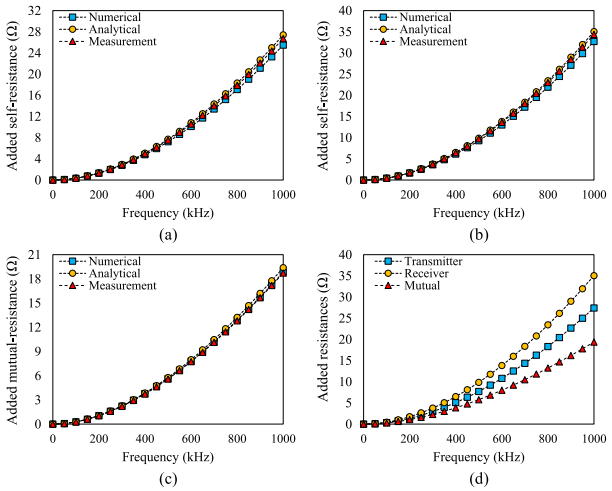

FIGURE 3. Additional resistances for the infinite medium. (a) Additional self-resistance of transmitter (b) Additional self-resistance of receiver (c) Mutual resistance (d) Overall comparison.

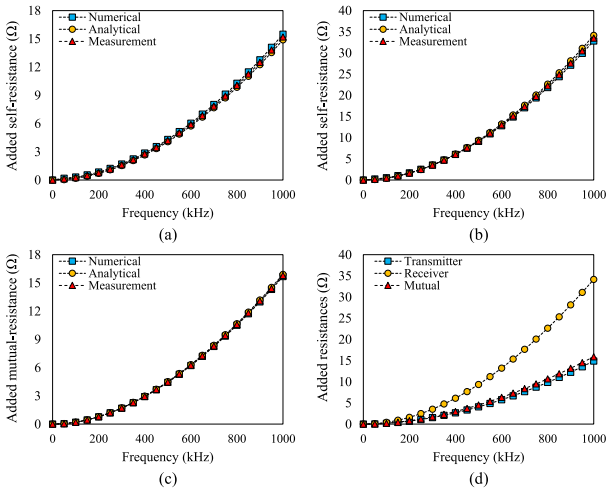

FIGURE 4. Additional resistances for the semi-finite medium. (a) Additional self-resistance of transmitter (b) Additional self-resistance of receiver (c) Mutual resistance (d) Overall comparison.

the derived formulas, the transmitter and receiver coils are different in geometry, leading to different additional resistances for each coil. The geometry of the coils and the electromagnetic characteristics of the conductive medium are listed in Table 1. The distance between coils is selected to be 10 cm. A container with dimensions of $60 \times 60 \times 40\,\text{cm}^3$ was selected for the measurements.

For the infinite medium where the coils are fully submerged in water, the additional resistances are depicted for the numerical, analytical, and measured results in Fig. 3, which confirms the high accuracy of the modeling. Increasing the frequency significantly increases both the additional self-resistances (Fig. 3(a) and (b)) and mutual-resistance (Fig. 3(c)), which in turn will dramatically increase the losses. Fig. 3(d) compares the overall observations of additional resistances in the infinite medium. Since the receiver coil has more turns, it exhibits higher additional resistance, and the mutual additional resistances for 10 cm distance of coils are lower than the additional self-resistances.

Fig. 4 illustrates the additional resistances observed in the semi-finite medium for various frequency values, where the medium is bounded on one side. Comparing Fig. 3 with Fig. 4, it is evident that the additional self-resistance of the transmitter coil has been decreased (Fig. 4(a)), while the additional self-resistance of the secondary coil has remained relatively unchanged (Fig. 4(b)). This indicates that, for the coupling distance of 10 cm, the electromagnetic characteristics of the first region have a minimal effect on the additional self-resistance of the receiving coil. Moreover, in Fig. 4(c) the additional mutual resistance has decreased, demonstrating the effect of removing the conductive medium from the first region on it. Fig. 4(d) compares all additional resistances in the semi-finite medium. Since the receiver coil is fully submerged, it exhibits higher additional resistance, with values close to those in the infinite medium. Additionally,

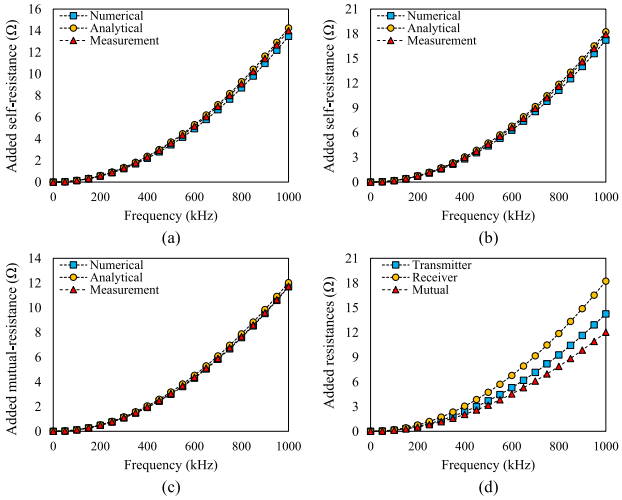

FIGURE 5. Additional resistances for the finite medium. (a) Additional self-resistance of transmitter (b) Additional self-resistance of receiver (c) Mutual resistance (d) Overall comparison.

when the first conductive region is removed, the additional resistance of the transmitter decreases and is closer to the mutual resistance.

For the finite medium, the additional resistances are compared in Fig. 5 for various frequency values, where the medium is bounded on both sides of the z-axis. The additional self-resistance of the receiver coil and the mutual resistance has been decreased compared to the infinite and semi-finite medium (Fig. 5(b), (c)). The transmitter coil experiences a smaller change in comparison to the semi-finite medium, indicating that removing the conductive medium from the third region has a minimal impact on the first coil Fig. 5(a). Similar to the infinite medium, the receiver coil exhibits higher additional resistance, and the mutual resistance values are the lowest (Fig. 5(d)).

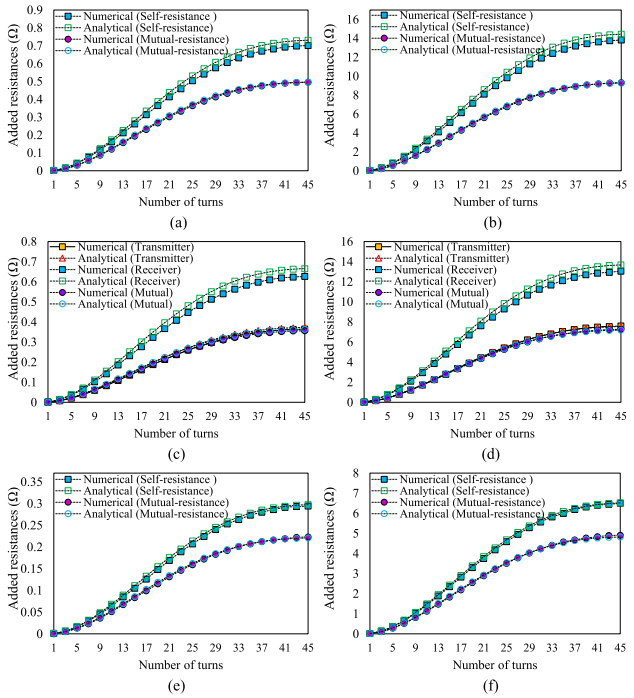

FIGURE 6. Comparison of the additional resistances for various number of turns at the frequency of 85 kHz and 400 kHz in each specific case. (a) Infinite medium at 85 kHz (b) Infinite medium at 400 kHz (c) Semi-finite medium at 85 kHz (d) Semi-finite medium at 400 kHz (e) Finite medium at 85 kHz (f) Finite medium at 400 kHz.

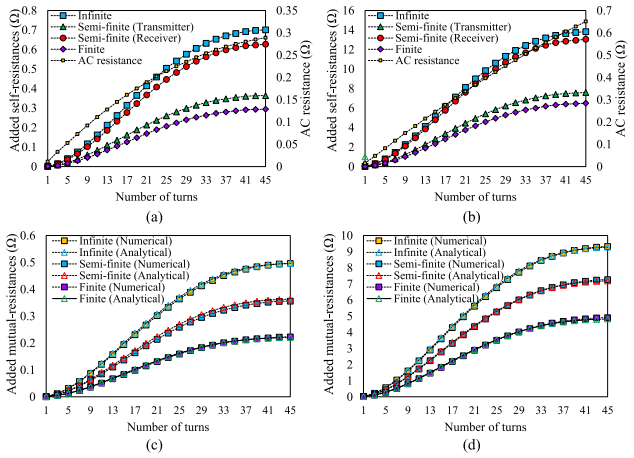

FIGURE 7. Additional resistances comparison for various number of turns at the frequency of 85 kHz and 400 kHz. (a) Additional self-resistances at 85 kHz (b) Additional self-resistances at 400 kHz (c) Additional mutual-resistances at 85 kHz (d) Additional mutual-resistances at 400 kHz.

B. GEOMETRICAL PARAMETERS VARIATION

The effect of changing the geometrical parameters of the coils on the additional resistance is explored through modeling and FEM. Figs. 6 and 7 illustrate the variations in additional resistances for different numbers of turns. These results are derived under the condition of a constant outer diameter of 250 mm and the frequency of 85 kHz and 400 kHz. The outermost current circle represents the first turn with a fixed diameter of 250 mm, and subsequent turns are twisting

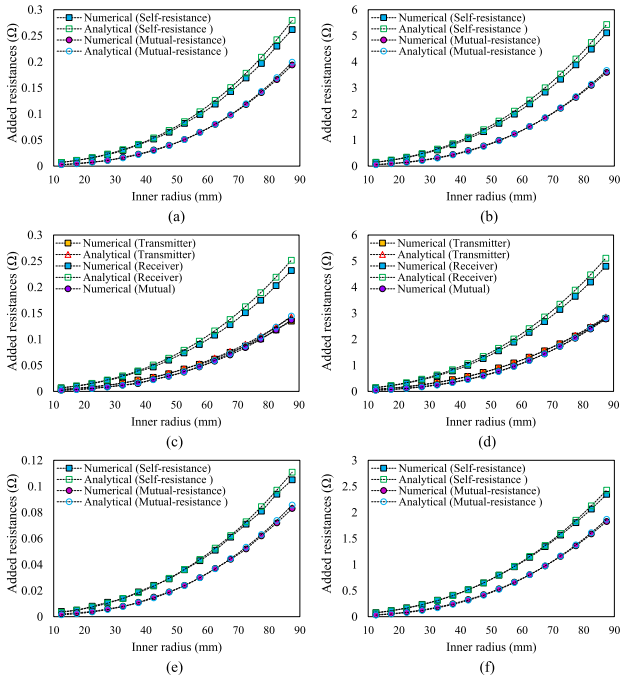

FIGURE 8. Comparison of the additional resistances for various values of the inner radius at the frequency of 85 kHz and 400 kHz in each specific case. (a) Infinite medium at 85 kHz (b) Infinite medium at 400 kHz (c) Semi-finite medium at 85 kHz (d) Semi-finite medium at 400 kHz (e) Finite medium at 85 kHz (f) Finite medium at 400 kHz.

inward towards the center of the coil. The spacing between turns is set to 1 mm. Additionally, both the transmitter and receiver share identical geometric configurations. Due to asymmetric boundary conditions in the semi-finite medium, the self-resistances of both transmitter and receiver coils are reported separately (Figs. 6(c) and (d)). Conversely, in both finite and infinite mediums, the self-resistances remain identical. For any number of turns, self-resistances are higher than mutual resistances, and at 400 kHz are much higher than at 85 kHz. These additional resistances have a higher value in the infinite medium and least in the finite medium. In the semi-finite medium for a coupling distance of 10 cm, mutual resistances closely mirror the additional self-resistance of the transmitter coil. Notably, in the semi-finite medium, where the receiving coil is fully immersed in water, its additional self-resistance surpasses that of the transmitter coil. Fig. 7 further differentiates the additional resistances with the AC self-resistances (air medium) of the coils. At the frequency of 85 kHz, the AC self-resistances are approximately equal to the additional self-resistance of the finite medium and the additional self-resistance of the transmitter coil in a semi-finite medium. However, the additional self-resistance of the receiver coil in the semi-finite medium and the additional self-resistances in the infinite medium are nearly twice the AC self-resistances. In contrast to 85 kHz, at the frequency of 400 kHz the AC self-resistances exhibit a linear increase with the number of turns, following a constant slope. However, the AC resistances are significantly smaller

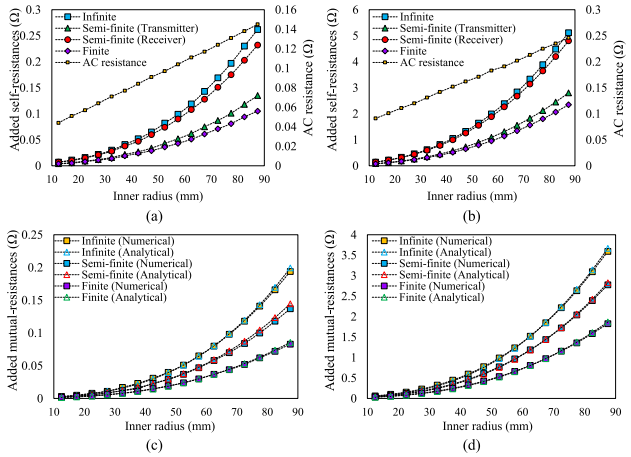

FIGURE 9. Additional resistances comparison for various values of the inner radius at the frequency of 85 kHz and 400 kHz. (a) Additional self-resistances at 85 kHz (b) Additional self-resistances at 400 kHz (c) Additional mutual-resistances at 85 kHz (d) Additional mutual-resistances at 400 kHz.

compared to the additional resistances in this frequency. Fig. 7(c) and (d) present the mutual added resistances, showcasing the lowest and highest values in the finite and infinite medium, respectively.

The impact of changes in the inner radius on additional resistances is illustrated in Figs. 8 and 9. The previous scenario is repeated, both the transmitter and receiver share identical geometric configurations. The number of turns is set to a fixed value of $N_t = N_r = 15$, and the spacing between turns is set at 1 mm. The comparison is made for both of the specified frequencies. For any value of inner radii, the self-resistances are higher than mutual resistances. AC resistances for both frequencies increase linearly with the increase of the inner radius of the coils. At the frequency of 85 kHz, the AC self-resistances are approximately equal to the additional self-resistance of the finite medium and the additional self-resistance of the transmitter coil in a semi-finite medium. However, the additional self-resistance of the receiver coil in the semi-finite medium and the additional self-resistances in the infinite medium are nearly twice the AC self-resistances.

The behavior of mutual inductances with additional self-resistances is compared in Fig. 10, revealing a similar trend in their increase with the number of turns, and inner radius. Importantly, inductances can be independently calculated regardless of the medium and the frequency. Hence, from Fig. 10 it can be predicted how the additional resistances will behave for desired inductances in the design process. This behavior was predictable, because from (18), inductances can be calculated independently, and analogous relationships to equations (20)-(22) can be derived, potentially exhibiting similar behavior. However, the calculation of inductances is not the focus of this study. Simpler formulas for inductance calculations exist in literature [14] and require significantly less computational effort than complex Bessel functions' improper integrals.

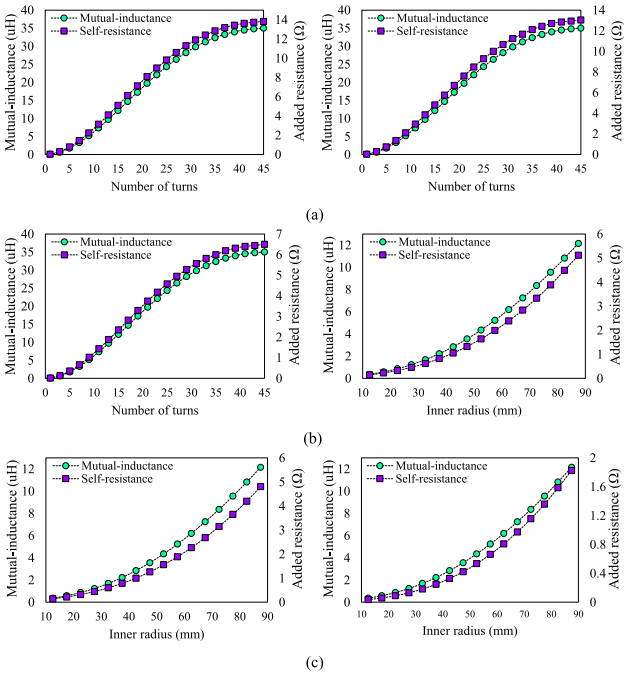

FIGURE 10. Comparison of additional resistances and mutual inductances for different numbers of turns and inner radii at the frequency of 400 kHz for each specific case: (a) Infinite medium (b) Semi-finite medium (c) Finite medium.

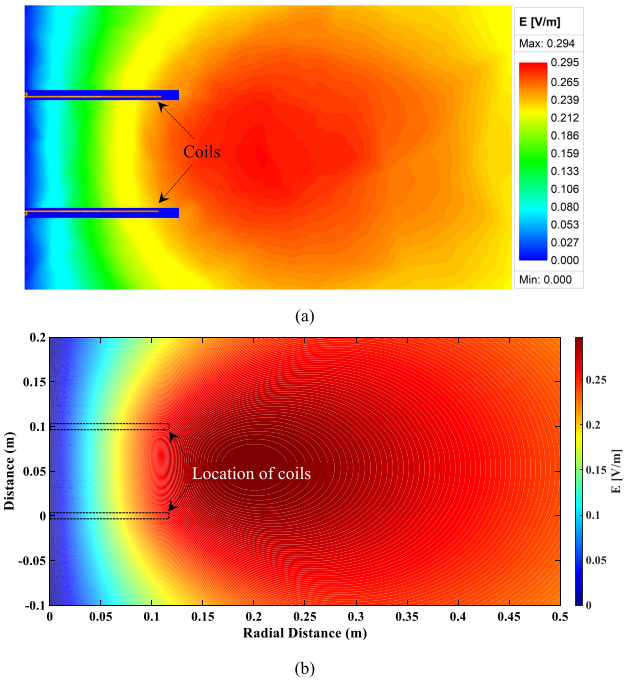

FIGURE 11. Electric field intensity distribution within the infinite water region, at the frequency of 85 kHz and applied current amplitudes of $I_t = I_r = 5A$ (a) FEM analysis (b) Analytical modeling.

C. ELECTRIC FIELD DISTRIBUTION

The comparison of how frequency, number of turns, and radius of turns affect additional resistances demonstrates that the modeling is highly accurate. Equations (20) to (22)

TABLE 2. Comparison of overall results of additional resistances and maximum electric field intensity, based on the parameters provided in Table 1.

		Infinite medium		Semi-finite medium		Finite medium	
	Frequency	Numerical	Analytical	Numerical	Analytical	Numerical	Analytical
Added resistance in transmitter coil (Ω)	85 kHz	0.246	0.261	0.126	0.133	0.100	0.104
	400 kHz	4.782	5.082	2.865	2.668	2.207	2.386
Added resistance in receiver coil (Ω)	85 kHz	0.315	0.334	0.279	0.301	0.128	0.133
	400 kHz	6.146	6.505	6.036	6.127	2.821	3.054
Mutual-resistance (Ω)	85 kHz	0.204	0.209	0.144	0.152	0.088	0.090
	400 kHz	3.779	3.854	2.925	2.974	1.930	2.056
Maximum electric field intensity (V/m)	85 kHz	0.294	0.298	0.215	0.231	0.128	0.132
	400 kHz	5.243	5.375	4.315	4.497	2.828	2.900

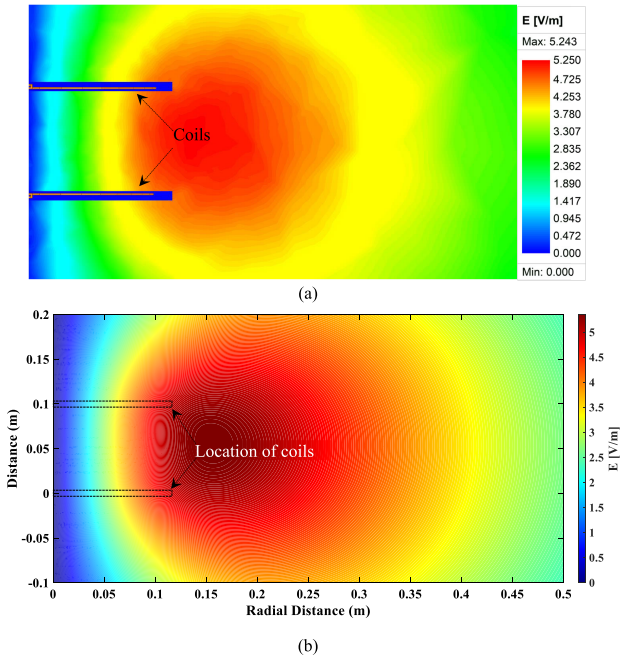

FIGURE 12. Electric field intensity distribution within the infinite water region, at the frequency of 400 kHz and applied current amplitudes of $I_t = I_r = 5A$ (a) FEM analysis (b) Analytical modeling.

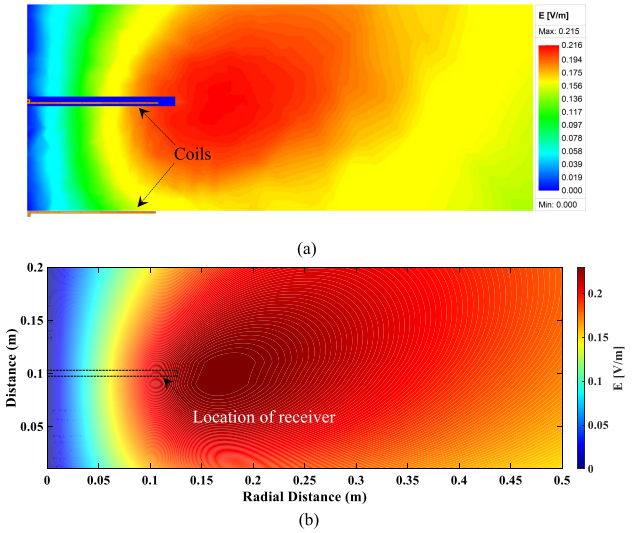

FIGURE 13. Electric field intensity distribution within the semi-finite water region, at the frequency of 85 kHz and applied current amplitudes of $I_t = I_r = 5A$ (a) FEM analysis (b) Analytical modeling.

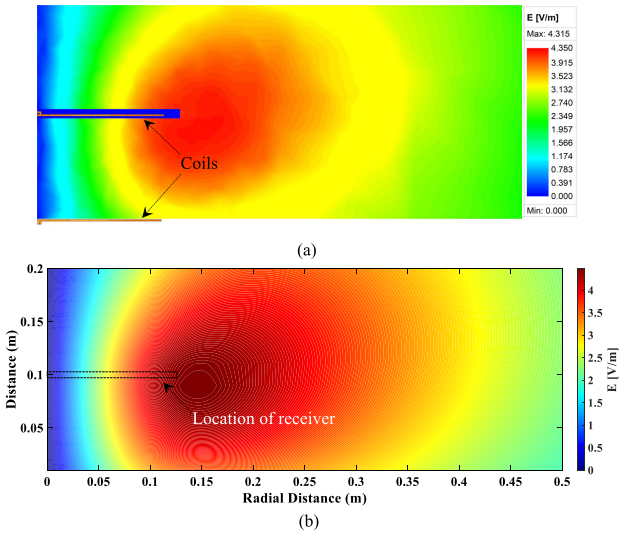

FIGURE 14. Electric field intensity distribution within the semi-finite water region, at the frequency of 400 kHz and applied current amplitudes of $I_t = I_r = 5A$ (a) FEM analysis (b) Analytical modeling.

can reliably predict additional resistances before the design process. For further analysis, the electric field distribution within the conductive medium is analyzed, highlighting that the circumferential component alone affects the electric field distribution and the corresponding resistances. To validate the model, the calculated plots are compared with FEM results at two different frequencies. The distribution of electric field intensities across all three case studies at both specified frequencies is illustrated in Figs. 11 to 16, showing that the electric field intensity increases with frequency. The electric field intensity comprises both real and imaginary components. Therefore, it is necessary to determine the component of the field that contributes to additional resistances. The results are obtained for the coils, with parameters detailed in Table 1. A cross-section of the YZ-plane or XZ-plane is considered to plot the electric field intensities. The amplitude of the applied currents to both coils is 5 A. For the infinite medium, by using (7)-(9) and (12) to (14), the electric field intensity in the conductive subregions is calculated separately. The results are then combined into a single plot, as shown in Figs. 11

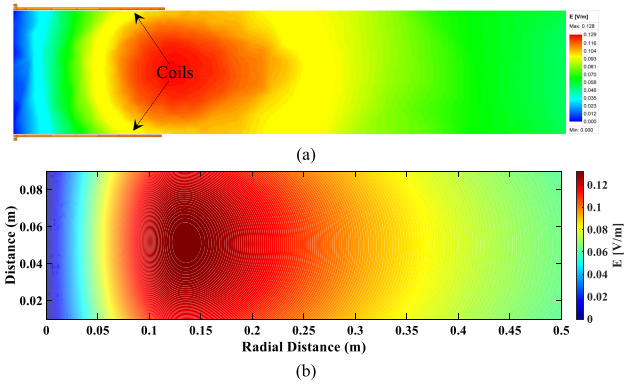

FIGURE 15. Electric field intensity distribution within the finite water region, at the frequency of 85 kHz and applied current amplitudes of $I_t = I_r = 5A$ (a) FEM analysis (b) Analytical modeling.

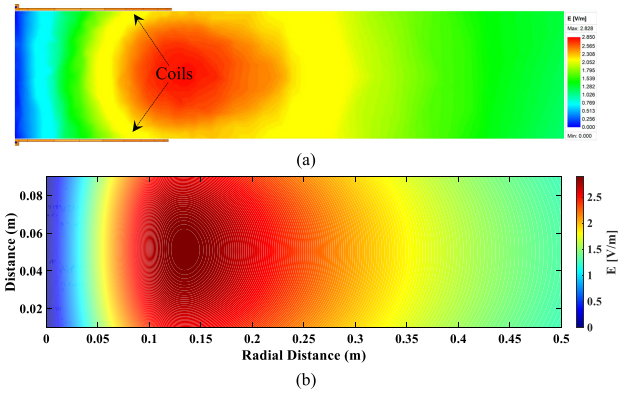

FIGURE 16. Electric field intensity distribution within the finite water region, at the frequency of 400 kHz and applied current amplitudes of $I_t = I_r = 5A$ (a) FEM analysis (b) Analytical modeling.

and 12. The comparison is conducted at frequencies of 85 kHz and 400 kHz. The maximum electric field intensities for frequencies of 85 kHz and 400 kHz are 0.294 V/m and 5.243 V/m, respectively, in the FEM analysis, and 0.298 V/m and 5.375 V/m in the modeling. The comparison highlights the high accuracy of the modeling in predicting electric field intensity. Using (8) and (9), the electric field intensities are calculated for the second and third regions of the semi-finite medium and then combined into a single plot, as shown in Figs. 13 and 14. In the case of the semi-finite medium, where the transmitter coil is above the water and the receiver is fully immersed, the high accuracy of the modeling is evident in these figures. The maximum field intensity occurs near the receiver coil, and are 0.215 V/m and 4.315 V/m, respectively, in the FEM simulation, and 0.231 V/m and 4.497 V/m in the analytical modeling. Finally, the electric field intensity in the finite medium is depicted in Figs. 15 and 16. The electric field intensity is calculated only for the middle region, where the maximum field intensities for the frequencies of 85 kHz and 400 kHz are 0.128 V/m and 2.828 V/m in the FEM analysis, and 0.132 V/m and 2.900 V/m in the analytical modeling, respectively. As seen, the electric field intensity decreases as the medium transitions from infinite (Fig. 2(a)) to semi-finite and finite in Fig. 2(c). This trend indicates that each region significantly impacts the electric field intensity. Table 2 presents an overall comparison of electric field intensity and additional resistances for the 10 cm distance at two different frequencies. By gradually moving from fully submerged coils to the conditions in Fig. 2(c), the additional resistances and electric field intensities decrease. The numerical results are slightly lower than the analytical results for both electric field intensity and additional resistances. In both infinite and semi-infinite environments, where the receiver coil is submerged in water, the additional resistance values are close to each other. In contrast, in finite and semi-finite medium, where the transmitter coil is outside the water, the additional resistance values are also close.

V. CONCLUSION

This study investigated the effect of eddy currents in the water environment on a pair of coaxial coils with the circular planar configuration. The surrounding conductive medium, separated by coils into three subregions, each region was assumed to have its own distinct electromagnetic properties. The electric field intensities were calculated in the cylindrical coordinate system by solving the Helmholtz equation in each region. The general formulas for additional self-resistances and mutual resistance rising from the water eddy currents, for any number of turns in the transmitter and receiver coils were derived. The formulas reflect each region's electromagnetic properties and geometrical parameters of each coil. The derived general formulas were applied to three different conditions that commonly occur in underwater applications. The results demonstrated high accuracy in modeling of electric field intensities and additional resistances in all three case studies. The equations accurately predict the eddy current effect when the coils are aligned; however, more comprehensive formulas are needed for the unaligned position, which frequently occurs in water environments.

REFERENCES

[1] C. Yang, M. Lin, and D. Li, "Improving steady and starting characteristics of wireless charging for an AUV docking system," *IEEE J. Ocean. Eng.*, vol. 45, no. 2, pp. 430–441, Apr. 2020.
[2] C. R. Teeneti, T. T. Truscott, D. N. Beal, and Z. Pantic, "Review of wireless charging systems for autonomous underwater vehicles," *IEEE J. Ocean. Eng.*, vol. 46, no. 1, pp. 68–87, Jan. 2021.
[3] J. Xu, X. Li, H. Li, Z. Xie, and Q. Ma, "Maximum efficiency tracking for multitransmitter multireceiver wireless power transfer system on the submerged buoy," *IEEE Trans. Ind. Electron.*, vol. 69, no. 2, pp. 1909–1919, Feb. 2022.
[4] K. Zhang, X. Zhang, Z. Zhu, Z. Yan, B. Song, and C. C. Mi, "A new coil structure to reduce eddy current loss of WPT systems for underwater vehicles," *IEEE Trans. Veh. Technol.*, vol. 68, no. 1, pp. 245–253, Jan. 2019.
[5] J. Wang, B. Song, and Y. Wang, "A method to reduce eddy current loss of underwater wireless power transmission by current control," *Appl. Sci.*, vol. 12, no. 5, p. 2435, Feb. 2022.
[6] M. Tamura, Y. Naka, K. Murai, and T. Nakata, "Design of a capacitive wireless power transfer system for operation in fresh water," *IEEE Trans. Microw. Theory Techn.*, vol. 66, no. 12, pp. 5873–5884, Dec. 2018.
[7] S. S. H. Yazdi, S. Shafiei, A. Kapanov, Y. Shakhin, A. Namadmalan, and M. Bagheri, "Enhanced domino wireless power transfer for transmission line monitoring: Overcoming external metal object interference and optimizing coil design," *IEEE Trans. Power Del.*, vol. 39, no. 2, pp. 1137–1150, Apr. 2024.

[8] K. Zhang, L. Du, Z. Zhu, B. Song, and D. Xu, "A normalization method of delimiting the electromagnetic hazard region of a wireless power transfer system," *IEEE Trans. Electromagn. Compat.*, vol. 60, no. 4, pp. 829–839, Aug. 2018.
[9] J. Kim, K. Kim, H. Kim, D. Kim, J. Park, and S. Ahn, "An efficient modeling for underwater wireless power transfer using Z-parameters," *IEEE Trans. Electromagn. Compat.*, vol. 61, no. 6, pp. 2006–2014, Dec. 2019.
[10] K. Zhang, Y. Ma, Z. Yan, Z. Di, B. Song, and A. P. Hu, "Eddy current loss and detuning effect of seawater on wireless power transfer," *IEEE J. Emerg. Sel. Topics Power Electron.*, vol. 8, no. 1, pp. 909–917, Mar. 2020.
[11] Z. Yan, Y. Zhang, T. Kan, F. Lu, K. Zhang, B. Song, and C. C. Mi, "Frequency optimization of a loosely coupled underwater wireless power transfer system considering eddy current loss," *IEEE Trans. Ind. Electron.*, vol. 66, no. 5, pp. 3468–3476, May 2019.
[12] J. Zhou, D.-J. Li, and Y. Chen, "Frequency selection of an inductive contactless power transmission system for ocean observing," *Ocean Eng.*, vol. 60, pp. 175–185, Mar. 2013.
[13] J. J. David, *Classical Electrodynamics*. Hoboken, NJ, USA: Wiley, 2021.
[14] S. Liu, J. Su, J. Lai, J. Zhang, and H. Xu, "Precise modeling of mutual inductance for planar spiral coils in wireless power transfer and its application," *IEEE Trans. Power Electron.*, vol. 36, no. 9, pp. 9876–9885, Sep. 2021.

SADJAD SHAFIEI was born in Incheh, Iran, in 1990. He received the B.Sc. degree in electrical power engineering from the University of Zanjan, Zanjan, Iran, in 2014, and the M.Sc. degree in electrical power engineering from the Amirkabir University of Technology (Tehran Polytechnic), Tehran, Iran, in 2020. He is currently working as a Research Assistant with the Smart Energy Systems Laboratory, School of Engineering and Digital Sciences, Nazarbayev University, Astana, Kazakhstan. His research interests include electromagnetics, wireless power transfer, and electrical machines.

SEYED SAEID HEIDARI YAZDI was born in Tabriz, Iran, in 1990. He received the B.Sc. degree in electrical power engineering from the Khajeh Nasir Toosi University of Technology, Tehran, Iran, in 2011, and the M.Sc. and Ph.D. degrees (Hons.) in electrical power engineering from the Amirkabir University of Technology, Tehran, in 2013 and 2019, respectively. Since June 2021, he has been working as a Postdoctoral Research Assistant in electrical power engineering with Nazarbayev University. His research interests include application of power electronics in HVDC grids, wireless electric power transfer systems, wind systems, energy storage systems, modern power systems, and the modeling and grid integration of renewable energy sources and power system control.

NURTAS ADAIKHAN received the master's degree in physics from Kazakh National University, with a focus on digital modulation and demodulation of chaotic signals. He is currently pursuing the Ph.D. degree in finite-time control problems for high-order nonlinear systems using state/output feedback with L. N. Gumilyov Eurasian National University, Astana. Since 2011, he has been working as a Physics Teacher with Nazarbayev Intellectual School (NIS) of Physics and Mathematics, Astana, where he also led the Department of Physics, from 2017 to 2019. He is a trained STEM robotics trainer and has contributed to the "catch-up and robotic7" program. He has collaborated with Cambridge University on educational programs and serves as a Principal Examiner for NIS Assessments.

MEHDI BAGHERI (Senior Member, IEEE) received the Ph.D. degree in electrical power engineering and energy systems from the University of New South Wales (UNSW), Sydney, Australia, in 2014. He was at the Electric Machinery and Drive Laboratory, Department of Electrical Engineering, National University of Singapore (NUS), and closely involved at the Rolls-Royce Pte., Ltd., on a joint project. Since 2016, he has been working with Nazarbayev University, where he is currently working as an Associate Professor with the Department of Electrical and Computer Engineering. He is also the Head of Smart Energy Systems Laboratory. He is actively involved in the advanced testing of industrial projects, and he provides technical support to multinational companies, specializing in power product manufacturing, strategic relationships between industry and academia, energy management, smart monitoring of power equipment, and analysis and development of sustainable energy systems. His research interests include climate change and energy security, high voltage engineering, wireless power transfer, condition monitoring and assessment, diagnosis of energy equipment in the field, space, marine applications, electrical rotating machines, electrical insulation, power quality, and smart energy systems. He was a member of the National Research Council of Kazakhstan, from 2020 to 2023. He is a member of IEEE PES, IES, and DEIS. In recognition of his contributions to engineering, he received the Scopus Award, in 2022, and in recognition of his distinguished contribution to Kazakhstan science and education, he received the "Enbegi Ushin Medal" from Kazakhstan Ministry of Science and Education, in 2024. He is an Associate Editor of IEEE Access and the *Frontiers in Energy Research*.